Synthesis and Magnon Thermal Transport Properties of Spin Ladder $Sr_{14}Cu_{24}O_{41}$ Microstructures

Xi Chen, Jaehyun Kim, Qianru Jia, Sean E. Sullivan, Youming Xu, Karalee Jarvis, Jianshi Zhou, and Li Shi*

The spin ladder compound $(Sr,Ca,La)_{14}Cu_{24}O_{41}$ exhibits an incommensurate layered structure with strong antiferromagnetic coupling. Besides intriguing superconducting behavior, recent experiments on bulk $Sr_{14}Cu_{24}O_{41}$ single crystals have revealed a remarkable magnon thermal conductivity, which is the largest above 100 K among all known quantum magnets. Although bulk $(Sr,Ca,La)_{14}Cu_{24}O_{41}$ crystals have been synthesized and studied extensively, there have been few reports on the synthesis and magnon thermal transport investigation of their microstructures. Here, the synthesis and thermal transport properties of $Sr_{14}Cu_{24}O_{41}$ microrods are reported. Electron microscopy studies indicate that these microrods synthesized by a coprecipitation method are single crystals grown preferentially along the ladder axis. Based on a four-probe thermal transport measurement, the thermal conductivity of the microrods reveals appreciable magnon transport in the microstructures. According to a kinetic model analysis, magnon transport in the microrods is suppressed mainly by increased point defect scattering compared to the bulk crystals, whereas surface scattering is negligible for anisotropic 1D magnon transport along the ladder. Moreover, the thermal conductivity is enhanced after annealing as a result of reduced oxygen vacancies. These results help to build the foundation for future heterogeneous integration of magnetic microstructures in microscale devices for the transport of energy and quantum information.

1. Introduction

Heat in materials can be carried by different types of particles or quasiparticles, including phonons, charge carriers, and magnetic excitations. Although thermal transport by phonons and charge carriers has been extensively investigated,[1,2] magnetic thermal transport remains to be better understood. Recently, thermal transport in some low-dimensional (low-D) quantum magnetic systems has attracted increasing interest.[3,4] Including 1D spin chains, spin ladders, and 2D quantum magnets, these low-D systems usually exhibit 180° Cu—O—Cu bond configuration that facilitates the superexchange interaction. The magnetic excitations in these systems are referred to as magnons in spin ladders and spinons in spin chains. Theoretical calculations predicted divergent thermal transport in the 1D spin-1/2 Heisenberg model as a result of its integrability.[5] In real materials, the magnetic excitations can couple with phonons, electrons, and defects, leading to a finite thermal conductivity (κ). Thermal transport measurements on spin ladder[6–8] and spin chain[9–12] systems have indeed observed a substantial and anisotropic magnetic contribution (κ_M) to the thermal conductivity. The κ in the direction parallel to the spin chains or ladders largely exceeds the κ in the directions perpendicular to it. Therefore, the analysis of κ_M can provide important information about the spin transport processes and energy dissipation length scales.[13]

Among these low-D quantum magnets, one prominent example is the spin ladder compound $Sr_{14}Cu_{24}O_{41}$ with a

Dr. X. Chen,[+] Dr. S. E. Sullivan,[++] Dr. K. Jarvis, Prof. J. S. Zhou, Prof. L. Shi
Materials Science and Engineering Program
Texas Materials Institute
The University of Texas at Austin
Austin, TX 78712, USA
E-mail: lishi@mail.utexas.edu

Prof. X. Chen, Y. M. Xu
Department of Electrical and Computer Engineering
University of California
Riverside, CA 92521, USA

Dr. J. Kim,[+++] Q. R. Jia
Department of Mechanical Engineering
The University of Texas at Austin
Austin, TX 78712, USA

[+]Present address: Department of Electrical and Computer Engineering, University of California, Riverside, CA 92521, USA

[++]Present address: Center for Molecular Engineering and Materials Science Division, Argonne National Laboratory, Lemont, IL 60439, USA

[+++]Present address: Department of Mechanical and Design Engineering, Hongik University, Sejong 30016, Republic of Korea

strong antiferromagnetic coupling energy J of $\approx$2000 K.[3] The Ca-doped spin ladder compound exhibits superconductivity under high pressure.[14] Recently, long-distance entanglement of spins in this compound has been observed via low-temperature magnetization and specific heat studies.[15] Besides these interesting superconductivity and spin properties, the κ along the spin ladder direction exhibits an additional broad peak near 140 K with the maximum value of about 100 W m^{-1} K^{-1}, which is attributed to the contribution from magnons.[16] These magnons are excited on the rung of spin ladders by flipping one of the spins to form a triplet spin state. Although triplets can propagate along the ladder, their correlations decay exponentially due to the finite spin energy gap (Δ) of about 33 meV.[17] The dispersion relation of triplets can be described as $\varepsilon^2(Q_c) = \Delta^2 + C^2 \sin^2(Q_c c_L)$, where ε is energy, C is the band maximum, Q_c is momentum along the spin ladder, and c_L is the lattice parameter of the ladders along the c-axis.[18] Inelastic neutron scattering measurements have identified a steep triplet dispersion, suggesting much higher group velocities of magnons than those of the acoustic phonons.[18,19] The large and anisotropic κ_M provides an approach to enhance thermal transport in the complex structures,[20,21] which typically possess small lattice thermal conductivity (κ_L) due to the presence of numerous optical phonon dispersions with low group velocities.[22] In addition, the large κ_M contribution is insensitive to magnetic fields up to 14 T since the magnon gap is much larger than the Zeeman energy.[16]

Previous studies of Sr$_{14}$Cu$_{24}$O$_{41}$ have focused on bulk single crystals. It has been found that magnon–hole scattering is important in this system. Through an isovalent substitution of Ca for Sr, the hole concentration is increased in the ladders due to a redistribution of holes between the chain and ladder sublattices,[23] leading to a suppressed κ_M in Sr$_{14}$Cu$_{24}$O$_{41}$.[16,24] On the other hand, κ_M can be significantly enhanced by replacing divalent Sr with trivalent La because of the reduction of hole concentration.[16,25] In addition, dynamic time-domain fluorescent flash measurements[26] and time-domain thermoreflectance (TDTR)[27] methods have been employed to study the phonon–magnon coupling in Ca$_9$La$_5$Cu$_{24}$O$_{41}$. Recently, textured polycrystalline Sr$_{14}$Cu$_{24}$O$_{41}$ samples were prepared by solid-state reaction followed by spark plasma sintering.[28] The magnon mean free path (MFP, l_M) of the textured samples was found to be reduced considerably at low temperatures. Such suppression of l_M can be explained by a defect scattering model of 1D magnons together with low transmission coefficients of 1D magnons across grain boundaries. In comparison to these active studies of single- and polycrystalline bulk magnetic structures, there have been few reports on the bottom-up synthesis and thermal transport characterization of magnetic microstructures, which can potentially be integrated heterogeneously with microscale devices for transporting heat and quantum information.[29–31]

Here, we report the synthesis and thermal transport study of Sr$_{14}$Cu$_{24}$O$_{41}$ microstructures, which are prepared by a coprecipitation synthesis. Transmission electron microscopy (TEM) studies indicate that these microrods are single crystals grown preferentially along the spin ladder axis. The temperature dependent κ of Sr$_{14}$Cu$_{24}$O$_{41}$ microstructures before and after annealing is measured by a four-probe thermal transport measurement method. The measurement results reveal the presence of appreciable magnon transport in the microrods, which is mainly suppressed compared to the bulk behavior by interior defects such as oxygen vacancies instead of surface roughness due to 1D anisotropic magnon thermal transport in the Sr$_{14}$Cu$_{24}$O$_{41}$ microrods. In addition, Raman, electron energy loss spectroscopy (EELS), and X-ray diffraction (XRD) measurement results further confirm an important role of oxygen vacancies on magnon thermal transport. These experimental findings represent an important initial step for the exploration of spin ladder microstructures as functional materials.

2. Results and Discussion

2.1. Phase and Microstructures

Figure 1a illustrates the crystal structure of Sr$_{14}$Cu$_{24}$O$_{41}$, which contains CuO$_2$ chains and Cu$_2$O$_3$ two-leg ladders. These two sublattices are incommensurate along the c-axis. Sr chains are present between the CuO$_2$ chains and Cu$_2$O$_3$ ladders, and are coordinated with the ladder sublattice to form Sr$_2$Cu$_2$O$_3$. The electron spins are aligned antiferromagnetically along the ladder sublattice. The microstructures of Sr$_{14}$Cu$_{24}$O$_{41}$ microrods were examined with scanning electron microscopy (SEM) and TEM. Electron dispersive X-ray spectroscopy (EDX) analysis confirms that the atomic ratio of microrods is in good agreement with the composition of Sr$_{14}$Cu$_{24}$O$_{41}$ (Figure S1, Supporting Information). The microrods exhibit a length ranging from 10 to 30 μm and a diameter of about 1–2 μm. Figure 1b shows a TEM image of a Sr$_{14}$Cu$_{24}$O$_{41}$ microrod synthesized at 760 °C. As shown in Figure 1c, the selected area electron diffraction (SAED) pattern is in agreement with that expected for an incommensurate spin ladder single crystal of CuO$_2$ chains and Sr$_2$Cu$_2$O$_3$ ladders,[32] thus confirming the single-crystalline nature of the microrod at least within the collimated electron beam. The growth direction is found to be along the c-axis, which is the high magnon thermal transport direction (Figure 1d). In addition, edge dislocations with an extra half-plane of atoms parallel to the c-axis are observed in the TEM, as displayed in Figure 1e and Figure S2 in the Supporting Information. Such extended defects have also been found in the Sr$_{14}$Cu$_{24}$O$_{41}$ polycrystals prepared by solid-state reaction.[28]

2.2. Thermal Conductivity Measurements

Figure 2a shows an optical image of the four-probe thermal transport measurement device. It consists of four suspended Au/Cr/SiN$_x$ lines, which act as microscale resistive heaters and thermometers. For a typical κ measurement, the Sr$_{14}$Cu$_{24}$O$_{41}$ microrod was transferred across the suspended lines, as shown in Figure 2b. The thermal resistance circuit of the measurement devices is displayed in Figure 2c. This measurement method can obtain both the intrinsic thermal resistance and the two extrinsic contact thermal resistances of the middle suspended sample segment. Such a four-probe method has been used to measure the κ of Si nanowires,[33] black
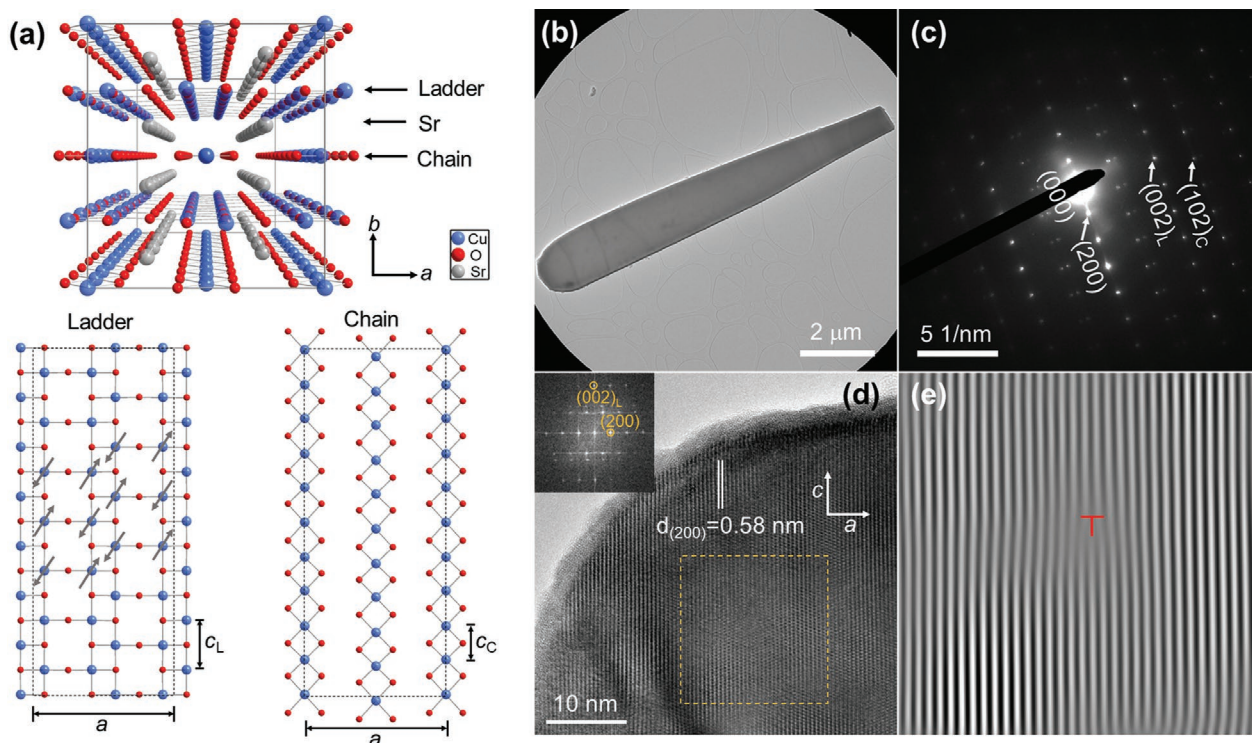
Figure 1. a) Crystal structure of $Sr_{14}Cu_{24}O_{41}$ consisting of two incommensurate sublattices. Partial spin alignment has been indicated by arrows in the ladder sublattice. b) TEM image of a $Sr_{14}Cu_{24}O_{41}$ microrod synthesized at 760 °C. c) SAED pattern of the $Sr_{14}Cu_{24}O_{41}$ microrod in (b) along the [010] zone axis indexed for the ladders (L) and chains (C) with both sharing the (200) planes. d) High resolution transmission electron microscopy (HRTEM) image taken on the tip of the $Sr_{14}Cu_{24}O_{41}$ microrod. The inset shows the fast Fourier transformation (FFT) pattern. e) The corresponding filtered inverse FFT of square area in (d) from (200) and ($\bar{2}$00) reflections. The red label indicates the location of the edge dislocation.
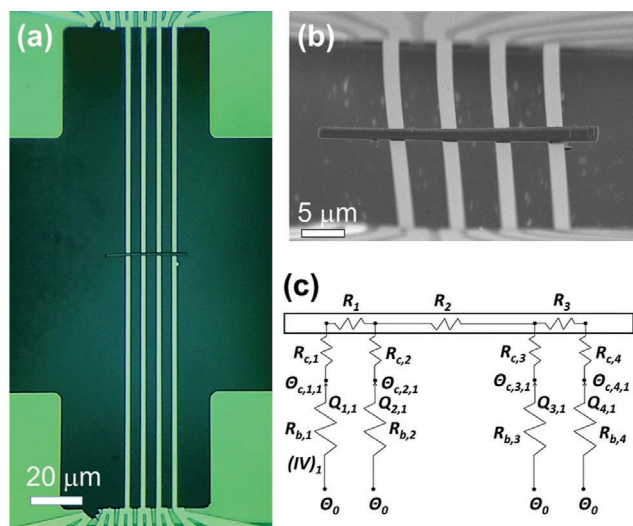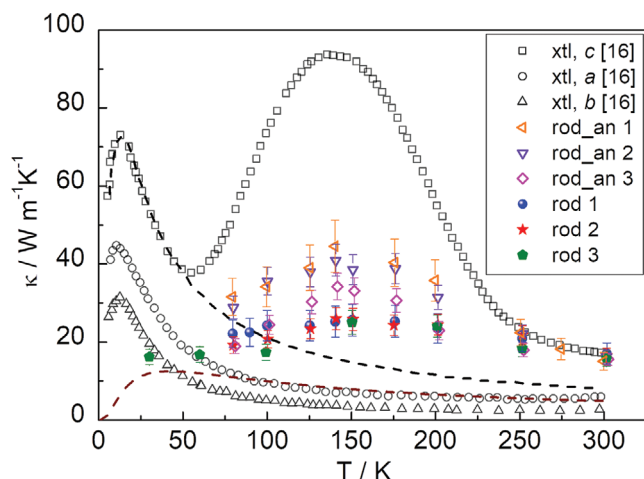

Figure 2. a) Optical micrograph of a $Sr_{14}Cu_{24}O_{41}$ microrod suspended on a four-probe thermal measurement device that consists of four suspended Au/Cr/SiN$_x$ beams. b) Tilted SEM image of the suspended $Sr_{14}Cu_{24}O_{41}$ microrod. c) Thermal resistance circuit of the $Sr_{14}Cu_{24}O_{41}$ sample. $R_{b,1}$, $R_{b,2}$, $R_{b,3}$, and $R_{b,4}$ are the thermal resistances of the four thermometer lines. R_1, R_2, and R_3 represent the thermal resistances of the left, middle, and right suspended segments of the $Sr_{14}Cu_{24}O_{41}$ rod. $R_{c,1}$, $R_{c,2}$, $R_{c,3}$, and $R_{c,4}$ are the contact thermal resistances at the four contacts to the sample. $\theta_{c,1}$, $\theta_{c,2}$, $\theta_{c,3}$, and $\theta_{c,4}$ are the thermometer temperature rises at the four contacts. θ_0 is the temperature rise at each end of each suspended thermometer line and is negligible.

phosphorus nanolayers,[34] BAs microstructures,[35] and MoS$_2$ nanolayers recently.[36] The four-probe thermal transport measurement method and its prior two-probe version have been used to measure low-D micro- and nanostructures with cross-section ranging from 1 nm² to 1 μm², thermal conductivity ranging between 0.1 and 3000 W m⁻¹ K⁻¹, and temperatures between 10 and 500 K.[37–39] Compared to prior two-probe measurement method, this new four-probe measurement approach has allowed us to eliminate the uncertainty arising from contact thermal resistance, which is important for samples with either a large κ or large diameter to length ratio. For this measurement to obtain accurate results, the thermal resistance of the suspended resistance thermometer lines needs to be designed to match the thermal resistance of the sample. This microscale thermal transport measurement method provides a unique probe of the magnons in the microstructures, which cannot be characterized readily with existing magnetic measurement techniques for bulk and thin film materials.

The thermal conductivity of $Sr_{14}Cu_{24}O_{41}$ microrods (**Figure 3**; Figure S5, Supporting Information) is calculated from the measured thermal resistance, R_2 (Figure 2c). In order to account for 3D heat conduction inside the microrod with a finite aspect ratio, numerical heat conduction simulation was carried out with the use of a finite element package (COMSOL) to calculate the conduction shape factor,[40,41] which has been used to convert the thermal resistance into thermal conductivity (Supporting Information). The κ of $Sr_{14}Cu_{24}O_{41}$ microrods exhibits a broad peak at low temperature, which is similar to that of the

**ADVANCED
SCIENCE NEWS**

www.advancedsciencenews.com

**ADVANCED
FUNCTIONAL
MATERIALS**

www.afm-journal.de

Figure 3. Thermal conductivity of $Sr_{14}Cu_{24}O_{41}$ microrods. Three microrod samples denoted as rod_an 1, 2, and 3 underwent an additional 940 °C annealing step compared to the other three samples denoted as rod 1, 2, and 3. The diameters of the microrods are 1.3 μm for rod 1, 1 μm for rod 2, 1.6 μm for rod 3, 1.2 μm for rod_an 1, 1.6 μm for rod_an 2, and 1.3 μm for rod_an 3. The single crystal (xtl) data reported in ref. [16] are shown as black open symbols and used for comparison with the data measured here for the microrods. The black dashed line is the fit to the low-temperature thermal conductivity data of the reported single crystal data along the c-axis with a Debye model of 3D phonon transport. The dark red dashed line represents the calculated lattice thermal conductivity along the c-axis for a sample with the phonon–boundary scattering mean free path of 1.3 μm and the other bulk scattering parameters.

single crystals along the c-axis.[16] However, the peak value of the microrods is reduced by more than half. The as-synthesized $Sr_{14}Cu_{24}O_{41}$ microrods exhibit a κ value of about 25 W m^{-1} K^{-1} at 140 K. For other samples grown from the same batch and undergoing an additional annealing step in air at 940 °C for 100 h, the measured κ is increased to the range between 35 and 45 W m^{-1} K^{-1} at 140 K.

2.3. Magnon Thermal Transport Analysis

In order to understand the magnon thermal transport in these $Sr_{14}Cu_{24}O_{41}$ microstructures, we first calculate the κ_L of the microrods. Since the magnon dispersion exhibits an energy gap of about 33 meV, κ_M is negligible below about 40 K.[24] Therefore, κ_L for the bulk crystal has been obtained by fitting the κ data reported in ref. [16] along the c-axis at temperatures below 40 K with the following Debye model for 3D phonon transport and extrapolating the fitting toward higher temperature[16,24]

$$\kappa_L = \frac{k_B}{2\pi^2 v}\left(\frac{k_B}{\hbar}\right)^3 T^3 \int_0^{\theta_D/T} \frac{x^4 e^x}{(e^x - 1)^2} \tau(\omega, T) \, dx \quad (1)$$
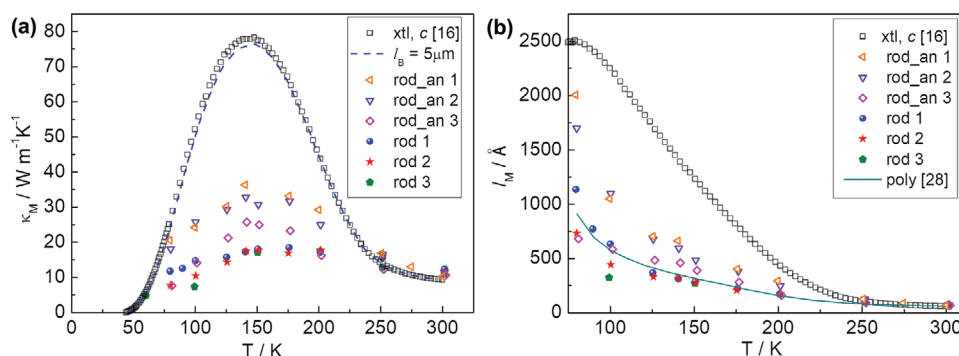
where k_B is Boltzmann constant, v is the sound velocity, T is temperature, θ_D is the Debye temperature, $\tau(\omega, T)$ is the phonon relaxation time, and $x = \hbar\omega/k_B T$. The phonon relaxation time is calculated as

$$\tau = \left[v/l_b + A\omega^4 + BT\omega^3 \exp(-\theta_D/CT)\right]^{-1} \quad (2)$$

where l_b is the phonon–boundary scattering mean free path, and A, B, and C are fitting parameters. The fit to Equation (1) is shown as the black dashed line in Figure 3. Diffuse phonon–boundary scattering and increased phonon–point defect scattering can reduce κ_L of the microrods. The Rayleigh scattering cross-section of atomic defects decreases with increasing phonon wavelength (λ) according to λ^{-4}.[42] Thus, phonon–defect scattering is dominated by phonon–boundary scattering in microstructures in the low temperature limit, where only long-λ, low-frequency phonons are populated. For a single-crystalline microrod, diffuse phonon–surface scattering reduces l_b to be the diameter (d).[42,43] By setting $l_b = d$ and retaining the bulk values for A, B, and C, we calculate κ_L for each rod (Figure S5a, Supporting Information). For rod 3 with $d = 1.3$ μm, the calculated κ_L is slightly lower than the measured κ at 30 K. The small difference can be caused by either a small magnon contribution or partially specular phonon–surface roughness scattering in the low-temperature limit, where the dominant phonon wavelength can be longer than the surface roughness asperity size. For the intermediate temperature range where the magnon contribution is appreciable, we expect phonon–surface scattering to be diffuse as the dominant phonon wavelength becomes comparable to or smaller than the nanometer-scale surface roughness shown in Figure 1d. In this intermediate temperature range, however, phonon–defect scattering can be appreciable compared to boundary scattering and phonon–phonon scattering. Hence, increased phonon–defect scattering in the microrods can reduce the actual κ_L in the intermediate temperature range below the calculated κ_L, which is the Casimir limit[43] and represents the upper limit of the microrods in the intermediate temperature range.

The κ_M is calculated by subtracting the calculated κ_L from the measured total κ, as displayed in **Figure 4**a. This process can underestimate κ_M in the intermediate temperature range due to the overestimated κ_L. As the temperature increases, the obtained κ_M first increases as a result of excitation of magnons above the spin gap, and then decreases due to the enhanced magnon–phonon scattering. It should be noted that the peak position of κ_M for $Sr_{14}Cu_{24}O_{41}$ microrods before annealing is about 170 K, while the peak position is reduced to about 140 K after annealing. Moreover, the κ_M of microrods is considerably smaller than that of the single crystal.[16] Annealing enhances the κ_M values markedly. At 140 K, the κ_M values are about 17 W m^{-1} K^{-1} for rod 1, 17 W m^{-1} K^{-1} for rod 2, and 17 W m^{-1} K^{-1} for rod 3 (at 150 K), while the κ_M values are increased to about 36 W m^{-1} K^{-1} for rod_an 1, 33 W m^{-1} K^{-1} for rod_an 2, and 26 W m^{-1} K^{-1} for rod_an 3. It should be noted that annealing can also increase the κ_L of the microrods due to a potential reduction of phonon–point defect scattering. However, the calculated κ_L of a 1.3 μm diameter microrod without considering additional defect scattering over the bulk value is about 8 W m^{-1} K^{-1} at 140 K. The κ_L change due to annealing should be much smaller than this upper limit, as well as the 9–19 W m^{-1} K^{-1} increase of κ upon annealing. Therefore, the κ enhancement after annealing is mainly attributed to the increased magnon contribution.

In order to better understand the magnon transport in $Sr_{14}Cu_{24}O_{41}$ microstructures, we calculate the average magnon

ADVANCED
SCIENCE NEWS
www.advancedsciencenews.com

ADVANCED
FUNCTIONAL
MATERIALS
www.afm-journal.de

Figure 4. a) Magnon thermal conductivity of $Sr_{14}Cu_{24}O_{41}$ microrods along the c-axis. The dashed line represents the κ_M calculated with magnon–boundary mean free path $l_B = 5$ μm along the c-axis and the other bulk scattering parameters. b) Calculated magnon MFP of $Sr_{14}Cu_{24}O_{41}$ microrods as a function of temperature. Shown for comparison is the magnon MFP of a bulk single crystal[16] and a bulk polycrystalline (poly) sample.[28]

mean free path based on a kinetic model for 1D magnon transport[16]

$$\kappa_M = \frac{3Nl_M}{\pi\hbar k_B T^2} \int_\Delta^{\varepsilon_{max}} \frac{\exp\left(\dfrac{\varepsilon}{k_B T}\right)}{\left[\exp\left(\dfrac{\varepsilon}{k_B T}\right)+3\right]^2} \varepsilon^2 d\varepsilon \qquad (3)$$

where N is the number of ladders per unit cross-section area perpendicular to the ladders, and ε_{max} is the band maximum of the dispersion. The occupation function (n_k) for triplets has a form of $n_k = 3/\left[\exp\left(\dfrac{\varepsilon}{k_B T}\right)+3\right]$,[16] which is used to account for the stringent constraint of no on-site double occupancy for the triplet excitations. The calculated l_M values are displayed in Figure 4b. The l_M of the single crystal along the c-axis is about 60 Å at 300 K, and increases to about 1400 Å at 140 K. With reference to the bulk values, l_M for the microrods is comparable at 300 K but reduced remarkably below 250 K. The l_M of the samples without annealing is about 300 Å at 140 K. After annealing, l_M is increased to 460–660 Å at 140 K.

Since magnon transport is 1D along the spin ladder axis and the microrods are single-crystalline based on the SAED result, surface or grain boundary scattering of magnons is not expected to be important in the microrods. To evaluate whether the reduced l_M is caused by magnon–boundary scattering at the two ends of the suspended segment, we include a magnon–boundary scattering MFP (l_B) in the total MFP according to Matthiessen's rule as[28]
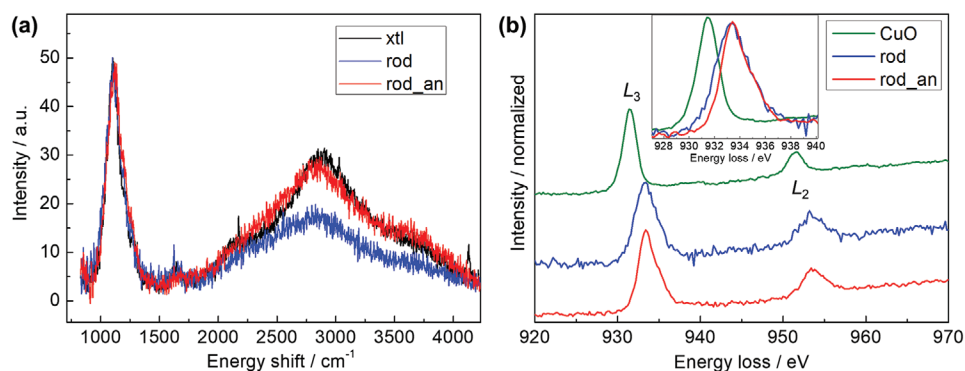
$$l_M^{-1} = l_{xtl}^{-1} + l_B^{-1} \qquad (4)$$

where l_{xtl} is the magnon MFP of single crystal along the c-axis as shown in Figure 4b. Without additional defect scattering, the κ_M for a sample with a l_B value of 5 μm along the c-axis does not change obviously as compared to single crystals, as shown in Figure 4a. The significant suppression of κ_M occurs when the l_B is smaller than 500 nm (Figure S6, Supporting Information). Based on a recent TDTR measurement on $Ca_9La_5Cu_{24}O_{41}$ crystals,[27] the magnon–phonon thermal relaxation length at 140 K is found to be about several hundred nanometers, which is much smaller than the separation of two nearby thermometer

lines in our κ measurements. Thus, the reduced κ_M and l_M in the $Sr_{14}Cu_{24}O_{41}$ microstructures is mainly caused by magnon–defect scattering instead of magnon–boundary scattering. In addition, the increased l_M due to annealing should be attributed to reduced defect concentration upon annealing. The different κ_M and l_M values obtained for different samples reflect a variation of the defect density in the samples. For example, the κ_M and l_M obtained for the rod_an 3 sample are smaller than those of other two annealed samples. This difference can be attributed to a higher defect concentration in the rod_an 3 sample. It is worth noting that both the κ_M and l_M of the samples without annealing are comparable to those of a polycrystalline bulk sample reported in a prior work.[28] Although the microrods are single crystalline with a much larger l_B than the 200 nm grain size of the bulk polycrystalline sample, the defect concentration in the microrods is expected to be higher than that in the bulk polycrystalline sample due to the lower synthesis temperature of the microrods.

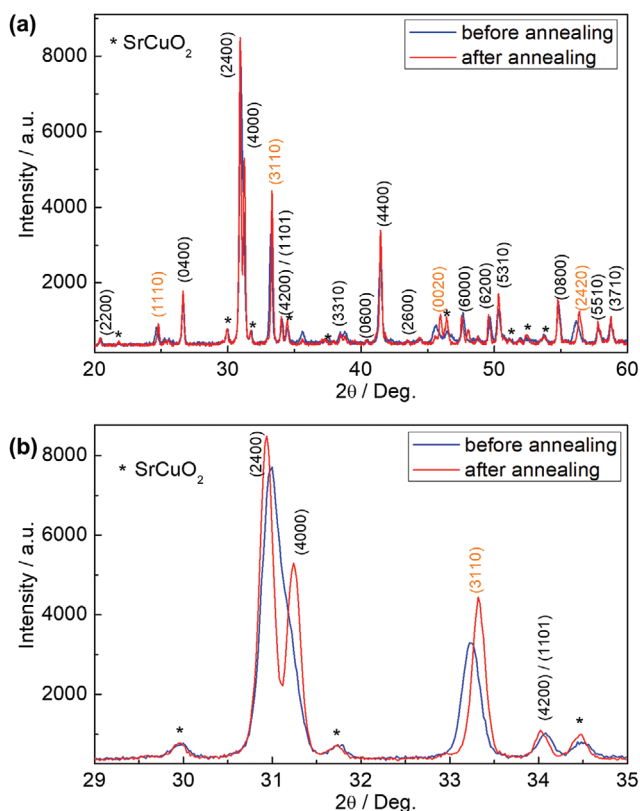### 2.4. Raman, EELS, and XRD Measurements of Defects

We further examine the nature of defects in as-synthesized microrods. Raman scattering measurements were performed on the microrods before and after annealing, as shown in **Figure 5**a. A broad peak is observed at about 2800 cm^{-1}, which is attributed to two-magnon scattering.[44] Two-magnon scattering originates from two magnons close to the Brillouin zone center with equal and opposite wavevector.[45] The microrods without annealing show a much smaller two-magnon peak as compared to the single crystals and annealed microrods. Such suppression of the two-magnon peak is also observed in other oxides with oxygen vacancies.[46] Furthermore, EELS was employed to observe changes to the oxidation state of Cu in the microrods before and after annealing. The EELS plot of the Cu-$L3$ and $L2$ edges is shown in Figure 5b. The edge onset of the $L3$ peak in the sample before annealing shifts to lower energies, toward the spectrum of CuO, compared with the annealed sample, indicating a lower oxidation state before annealing. Oxygen vacancies in the sample would result in a decrease of the average valence for Cu, in good agreement with our EELS results. Our finding is consistent with a prior report[47] on the

**ADVANCED
SCIENCE NEWS**

www.advancedsciencenews.com

**ADVANCED
FUNCTIONAL
MATERIALS**

www.afm-journal.de

Figure 5. a) Raman spectra of $Sr_{14}Cu_{24}O_{41}$ microrods before and after annealing together with the single crystal data excited by a 488 nm light. b) EELS plots of $Sr_{14}Cu_{24}O_{41}$ microrods before and after annealing. Shown for comparison is data of CuO.

high sensitivity of the oxygen stoichiometry in $Sr_{14}Cu_{24}O_{41}$ to high temperature annealing. In addition, we compare the XRD patterns of the powder samples before and after annealing (**Figure 6**). The diffraction peaks associated with the ladder sublattice shift to a higher angle after annealing, indicating the contraction of the ladder sublattice possibly due to the reduced oxygen vacancies. It should be noted that the presence of oxygen vacancies can cause lattice expansion through

Figure 6. a) XRD patterns of the $Sr_{14}Cu_{24}O_{41}$ powder samples before and after annealing. b) The zoomed in XRD pattern showing the shift of the peak associated with the ladder sublattice near 33°. All reflections are indexed using four indices ($h\,k\,l_L\,l_C$) in order to account for the two sublattices where the third index belongs to the ladders and the fourth to the chains.

electrostatic repulsion since positively charged cations are no longer shielded by negatively charged oxygen ions, as observed in some oxides.[48] In addition, a small amount of $SrCuO_2$ was observed in the XRD measurements of the mixture of microstructures from the synthesis. This impurity was formed as a result of Cu loss during the synthesis so that the actual ratio between Sr and Cu deviates from the ideal ratio, and increasing the amount of starting material $Cu(NO_3)_2 \cdot 2.5H_2O$ could potentially reduce the $SrCuO_2$ impurity. According to our TEM studies of single microrods, these microrods are single-crystalline $Sr_{14}Cu_{24}O_{41}$ without any secondary phase. Therefore, the $SrCuO_2$ phase in the mixture may occur in a small fraction of the microstructures that exhibit a different morphology due to the different crystal structure compared to the $Sr_{14}Cu_{24}O_{41}$ microrods. Together with the Raman, EELS, and XRD studies, it can be inferred that oxygen vacancies are formed in the as-synthesized $Sr_{14}Cu_{24}O_{41}$ microrods. These oxygen vacancies, which are mainly formed in the ladder sublattice, can lead to a deformation of the ladder in the vicinity of an oxygen vacancy. Such deformation modulates the exchange coupling in the ladder, resulting in scattering magnons and suppressing κ_M significantly. Upon annealing in air, the oxygen vacancy concentration is decreased, leading to an enhanced κ_M.

3. Conclusion

These experiments have demonstrated a coprecipitation method for the synthesis of single-crystalline $Sr_{14}Cu_{24}O_{41}$ microrods. The four-probe thermal transport measurement confirms the presence of appreciable 1D magnon transport along the microrod axis that is parallel to the spin ladder axis. The mangon thermal conductivity of these microrods is found to be suppressed as compared to bulk single crystals due to the presence of defects, including dislocations and oxygen vacancies, instead of the reduced cross-section. The magnon thermal conductivity can be enhanced significantly with high temperature annealing due to a reduction of the defect concentration. One type of defects in microrods is the oxygen vacancies, which change remarkably by annealing, as confirmed by Raman, EELS, and XRD studies. Together with the recent advance of pick-and-place techniques, the demonstrated bottom-up synthesis of magnetic microstructures may lead to functional

devices where these microstructures are heterogeneously integrated with other materials to transport quantum information and heat.

4. Experimental Section

Synthesis of $Sr_{14}Cu_{24}O_{41}$ Microrods: $Sr_{14}Cu_{24}O_{41}$ microrods were prepared by a coprecipitation method. The starting materials were strontium nitrate $Sr(NO_3)_2$, copper nitrate $Cu(NO_3)_2 \cdot 2.5H_2O$, and sodium carbonate Na_2CO_3. Initially, 0.005 mol $Sr(NO_3)_2$ and 0.0086 mol $Cu(NO_3)_2 \cdot 2.5H_2O$ were gradually added to 30 mL deionized water. The mixture was then stirred to form a solution. Next, 0.0136 mol Na_2CO_3 dissolved in 30 mL deionized water was added to the $Sr(NO_3)_2$ and $Cu(NO_3)_2 \cdot 2.5H_2O$ solution and continuously stirred for about 10 min until the blue precipitant was formed. The precipitant was collected by filtering in vacuum system and washed with deionized water. The precipitant was then calcined in air at 760 °C for 70 h. To study the effect of defects on κ, the obtained power samples were annealed in air at 940 °C for 100 h.

Characterization: The phase and crystal structure of the samples were studied by XRD with a Philips X'pert diffractometer with Cu Kα radiation ($\lambda = 1.54184$ Å). The microstructures of the microrods were analyzed by using a Quanta 600 environmental SEM and a JEOL 2010F TEM. The EELS data were acquired on the JEOL 2010F TEM at 200 kV using a Gatan Enfina spectrometer. For comparison, an electron energy loss (EEL) spectrum for CuO was collected on the same instrument and with identical parameters as the samples. EEL spectra were calibrated to the carbon peak from the lacey carbon sample grid. Raman spectroscopy was utilized to probe the phonon and magnon peaks of the samples at room temperature using a 488 nm probe laser. The thermal conductivity of the $Sr_{14}Cu_{24}O_{41}$ samples in the temperature interval between about 30 and 300 K was measured by a four-probe thermal transport measurement method.[33]

Supporting Information

Supporting Information is available from the Wiley Online Library or from the author.

Conflict of Interest

The authors declare no conflict of interest.

Keywords

[1] E. S. Toberer, L. L. Baranowski, C. Dames, *Annu. Rev. Mater. Res.* **2012**, *42*, 179.

[2] S. Shin, Q. Wang, J. Luo, R. Chen, *Adv. Funct. Mater.* **2020**, *30*, 1904815.

[3] C. Hess, *Eur. Phys. J.: Spec. Top.* **2007**, *151*, 73.

[4] A. V. Sologubenko, T. Lorenz, H. R. Ott, A. Freimuth, *J. Low Temp. Phys.* **2007**, *147*, 387.

[5] X. Zotos, F. Naef, P. Prelovsek, *Phys. Rev. B* **1997**, *55*, 11029.

[6] A. V. Sologubenko, E. Felder, K. Giannò, H. R. Ott, A. Vietkine, A. Revcolevschi, *Phys. Rev. B* **2000**, *62*, R6108.

[7] C. Hess, H. ElHaes, B. Büchner, U. Ammerahl, M. Hücker, A. Revcolevschi, *Phys. Rev. Lett.* **2004**, *93*, 027005.

[8] C. Hess, P. Ribeiro, B. Büchner, H. ElHaes, G. Roth, U. Ammerahl, A. Revcolevschi, *Phys. Rev. B* **2006**, *73*, 104407.

[9] A. V. Sologubenko, K. Giannò, H. R. Ott, A. Vietkine, A. Revcolevschi, *Phys. Rev. B* **2001**, *64*, 054412.

[10] N. Hlubek, P. Ribeiro, R. Saint-Martin, A. Revcolevschi, G. Roth, G. Behr, B. Büchner, C. Hess, *Phys. Rev. B* **2010**, *81*, 020405.

[11] N. Hlubek, P. Ribeiro, R. Saint-Martin, S. Nishimoto, A. Revcolevschi, S. L. Drechsler, G. Behr, J. Trinckauf, J. E. Hamann-Borrero, J. Geck, B. Büchner, C. Hess, *Phys. Rev. B* **2011**, *84*, 214419.

[12] X. Chen, J. Carrete, S. Sullivan, A. van Roekeghem, Z. Li, X. Li, J. Zhou, N. Mingo, L. Shi, *Phys. Rev. Lett.* **2019**, *122*, 185901.

[13] C. Hess, C. Baumann, B. Büchner, *J. Magn. Magn. Mater.* **2005**, *290–291*, 322.

[14] M. Uehara, T. Nagata, J. Akimitsu, H. Takahashi, N. Môri, K. Kinoshita, *J. Phys. Soc. Jpn.* **1996**, *65*, 2764.

[15] S. Sahling, G. Remenyi, C. Paulsen, P. Monceau, V. Saligrama, C. Marin, A. Revcolevschi, L. P. Regnault, S. Raymond, J. E. Lorenzo, *Nat. Phys.* **2015**, *11*, 255.

[16] C. Hess, C. Baumann, U. Ammerahl, B. Büchner, F. Heidrich-Meisner, W. Brenig, A. Revcolevschi, *Phys. Rev. B* **2001**, *64*, 184305.

[17] T. Vuletić, B. Korin-Hamzić, T. Ivek, S. Tomić, B. Gorshunov, M. Dressel, J. Akimitsu, *Phys. Rep.* **2006**, *428*, 169.

[18] R. S. Eccleston, M. Uehara, J. Akimitsu, H. Eisaki, N. Motoyama, S.-i. Uchida, *Phys. Rev. Lett.* **1998**, *81*, 1702.

[19] X. Chen, D. Bansal, S. Sullivan, D. L. Abernathy, A. A. Aczel, J. Zhou, O. Delaire, L. Shi, *Phys. Rev. B* **2016**, *94*, 134309.

[20] M. Otter, G. Athanasopoulos, N. Hlubek, M. Montagnese, M. Labois, D. A. Fishman, F. de Haan, S. Singh, D. Lakehal, J. Giapintzakis, C. Hess, A. Revcolevschi, P. H. M. van Loosdrecht, *Int. J. Heat Mass Transfer* **2012**, *55*, 2531.

[21] T. Feng, X. Wu, X. Yang, P. Wang, L. Zhang, X. Du, X. Wang, S. T. Pantelides, *Adv. Funct. Mater.* **2020**, *30*, 1907286.

[22] X. Chen, A. Weathers, J. Carrete, S. Mukhopadhyay, O. Delaire, D. A. Stewart, N. Mingo, S. N. Girard, J. Ma, D. L. Abernathy, *Nat. Commun.* **2015**, *6*, 6723.

[23] N. Nücker, M. Merz, C. A. Kuntscher, S. Gerhold, S. Schuppler, R. Neudert, M. S. Golden, J. Fink, D. Schild, S. Stadler, V. Chakarian, J. Freeland, Y. U. Idzerda, K. Conder, M. Uehara, T. Nagata, J. Goto, J. Akimitsu, N. Motoyama, H. Eisaki, S. Uchida, U. Ammerahl, A. Revcolevschi, *Phys. Rev. B* **2000**, *62*, 14384.

[24] A. Sologubenko, K. Gianno, H. Ott, U. Ammerahl, A. Revcolevschi, *Phys. Rev. Lett.* **2000**, *84*, 2714.

[25] K. Naruse, T. Kawamata, M. Ohno, Y. Matsuoka, K. Kumagai, Y. Koike, *Solid State Commun.* **2013**, *154*, 60.

[26] M. Montagnese, M. Otter, X. Zotos, D. A. Fishman, N. Hlubek, O. Mityashkin, C. Hess, R. Saint-Martin, S. Singh, A. Revcolevschi, P. H. M. van Loosdrecht, *Phys. Rev. Lett.* **2013**, *110*, 147206.

[27] G. T. Hohensee, R. B. Wilson, J. P. Feser, D. G. Cahill, *Phys. Rev. B* **2014**, *89*, 024422.

[28] X. Chen, K. Jarvis, S. Sullivan, Y. Li, J. Zhou, L. Shi, *Phys. Rev. B* **2017**, *95*, 144310.

[29] A. Singh, C. Jansen, K. Lahabi, J. Aarts, *Phys. Rev. X* **2016**, *6*, 041012.

[30] H. Zhang, D. E. Liu, M. Wimmer, L. P. Kouwenhoven, *Nat. Commun.* **2019**, *10*, 5128.

[31] H. Y. Yuan, M.-H. Yung, X. R. Wang, *Phys. Rev. Res.* **2019**, *1*, 033052.

[32] J. Wang, H. Zou, Y. Li, H. Xie, N. Hu, L. Wang, J. Shi, *Phys. B* **2014**, *441*, 6.

[33] J. Kim, E. Ou, D. P. Sellan, L. Shi, *Rev. Sci. Instrum.* **2015**, *86*, 044901.

[34] B. Smith, B. Vermeersch, J. Carrete, E. Ou, J. Kim, N. Mingo, D. Akinwande, L. Shi, *Adv. Mater.* **2017**, *29*, 1603756.

[35] J. Kim, D. A. Evans, D. P. Sellan, O. M. Williams, E. Ou, A. H. Cowley, L. Shi, *Appl. Phys. Lett.* **2016**, *108*, 201905.

[36] B. Smith, L. Lindsay, J. Kim, E. Ou, R. Huang, L. Shi, *Appl. Phys. Lett.* **2019**, *114*, 221902.

[37] L. Shi, D. Li, C. Yu, W. Jang, D. Kim, Z. Yao, P. Kim, A. Majumdar, *J. Heat Transfer* **2003**, *125*, 881.

[38] D. Li, Y. Wu, P. Kim, L. Shi, P. Yang, A. Majumdar, *Appl. Phys. Lett.* **2003**, *83*, 2934.

[39] J. H. Seol, I. Jo, A. L. Moore, L. Lindsay, Z. H. Aitken, M. T. Pettes, X. Li, Z. Yao, R. Huang, D. Broido, N. Mingo, R. S. Ruoff, L. Shi, *Science* **2010**, *328*, 213.

[40] R. Prasher, *Nano Lett.* **2005**, *5*, 2155.

[41] V. Bahadur, J. Xu, Y. Liu, T. S. Fisher, *J. Heat Transfer* **2005**, *127*, 664.

[42] J. M. Ziman, *Electrons and Phonons: The Theory of Transport Phenomena in Solids*, Oxford University Press, Oxford **2001**.

[43] H. B. G. Casimir, *Physica* **1938**, *5*, 495.

[44] S. Sugai, M. Suzuki, *Phys. Status Solidi B* **1999**, *215*, 653.

[45] A. Gozar, G. Blumberg, B. S. Dennis, B. S. Shastry, N. Motoyama, H. Eisaki, S. Uchida, *Phys. Rev. Lett.* **2001**, *87*, 197202.

[46] N. H. Sung, H. Gretarsson, D. Proepper, J. Porras, M. Le Tacon, A. V. Boris, B. Keimer, B. J. Kim, *Philos. Mag.* **2016**, *96*, 413.

[47] Z. Hiroi, S. Amelinckx, G. Van Tendeloo, N. Kobayashi, *Phys. Rev. B* **1996**, *54*, 15849.

[48] F. Heydari, A. Maghsoudipour, M. Alizadeh, Z. Khakpour, M. Javaheri, *Bull. Mater. Sci.* **2015**, *38*, 1009.

2001637 (8 of 8)